Theoretical predictions of the generalized contrast-to-noise ratio for photoacoustic images

Mardava R. Gubbi* and Muyinatu A. Lediju Bell*†‡
*Department of Electrical and Computer Engineering, Johns Hopkins University, Baltimore, MD
†Department of Computer Science, Johns Hopkins University, Baltimore, MD
‡Department of Biomedical Engineering, Johns Hopkins University, Baltimore, MD

***Abstract*—Target detectability in photoacoustic imaging applications is traditionally analyzed using image quality metrics, such as signal-to-noise ratio, contrast, and contrast-to-noise ratio. These metrics are difficult to interpret in the context of target detectability due to their lack of an upper bound and their sensitivity to image manipulation techniques such as thresholding. The generalized contrast-to-noise ratio (gCNR) is a recently introduced metric designed to assess the probability of lesion detection in ultrasound images. Previous work used empirical models of target and background signals to demonstrate the applicability of gCNR to analyzing target detectability in photoacoustic images. In this work, a theoretical framework for gCNR prediction is developed and validated using simulated, experimental, and *in vivo* data. We compare predicted and measured gCNR values across variations in channel SNR, laser energy, and frame averaging. Mean absolute errors between predicted and measured gCNR values were 0.032 $\pm$ 0.052, 0.057 $\pm$ 0.127, and 0.023 $\pm$ 0.033 for 1,215 simulated images, 3,888 experimental images, and 810 *in vivo* delay-and-sum images, respectively, with channel SNRs ranging -40 dB to 40 dB. In addition, we explored relationships among gCNR, laser energy, and channel data frame averaging. Results have the potential to improve our understanding of minimum energy requirements when designing photoacoustic imaging systems. In addition, the theoretical gCNR prediction framework provides a promising foundation to improve the efficiency of presurgical tasks such as energy selection for photoacoustic-guided surgeries.**

***Index Terms*—photoacoustic imaging, image processing**

I. Introduction

Target detectability in photoacoustic images is traditionally assessed using image quality metrics such as signal-to-noise ratio (SNR), contrast, and the contrast-to-noise ratio (CNR) [1], [2]. These metrics lack upper bounds, complicating their interpretation in the context of target detection. In addition, SNR, contrast, and CNR are sensitive to common image manipulation techniques such as dynamic range adjustment and thresholding, which may lead to an increase in these metrics without a corresponding improvement in target detectability [3].

The generalized contrast-to-noise ratio (gCNR) is a new image quality metric introduced to assess the probability of lesion detection in ultrasound images [4]. Rodriguez-Molares *et al.* [4] described gCNR as a measure of the accuracy of a two-class classifier operating on a given ultrasound image, then used this description to establish a theoretical framework to predict the gCNR of ultrasound images. This ultrasound-based framework is insufficient for photoacoustic images for three reasons. First, photoacoustic target signal characteristics differ from those of ultrasound targets. Second, photoacoustic targets typically have a higher optical absorption than the background. Third, the theoretical ultrasound framework is not equipped to solve the more complex decision boundaries which can arise in photoacoustic images.

Previous work by our group demonstrated the applicability of gCNR to photoacoustic images [5]. We used histograms representing the target and background characteristics to measure the gCNR of photoacoustic images. We demonstrated several advantages of gCNR over more traditional image quality metrics including ease of interpretation, smaller variations for fully detectable targets, and robustness to image manipulation techniques such as thresholding and dynamic range adjustment. However, no theoretical framework similar to [4] has been developed for photoacoustic images, and histogram-based measurements of gCNR are sensitive to parameters such as the width and positions of the histogram bins which affect the representation of the underlying target and background signals.

In this paper, we develop a theoretical gCNR prediction framework for photoacoustic images to overcome these challenges. We use the two-class classifier formulation of gCNR [4] and previously established models for photoacoustic target signals [6] and noise [7] to derive an expression for gCNR based on the photoacoustic signal characteristics of an image. We then investigate the match between predicted and measured gCNR values for simulated, experimental, and *in vivo* photoacoustic images across a range of channel SNR values. Finally, we use this framework to investigate the relationship among gCNR, frame averaging prior to delay-and-sum (DAS) beamforming, and laser energy.

II. Theory

Developing our theoretical framework to predict the gCNR of photoacoustic images requires an understanding of the gCNR framework for ultrasound images and the characteristics of photoacoustic target and background signals. Rodriguez-Molares *et al.* [4] describe gCNR as a normalized measure of the highest achievable probability of success of a two-class classifier operating on a given ultrasound image. The target and background signals are assumed to follow complex normal distributions, the target is assumed to be hypoechoic, and the target and background regions of interest (ROIs) are assumed

978-1-7281-5448-0/20/$31.00 ©2020 IEEE

Authorized licensed use limited to: Johns Hopkins University. Downloaded on January 14,2021 at 16:13:51 UTC from IEEE Xplore. Restrictions apply.

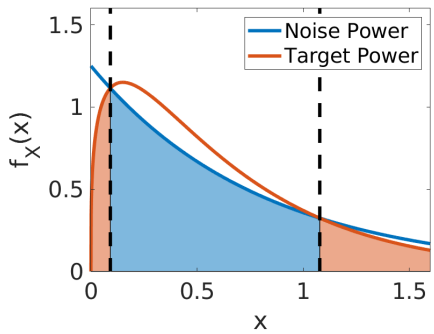

Fig. 1. Target and background power distributions extracted from a photoacoustic image, showing multiple points of intersection.

to have equal area. With these assumptions, gCNR is expressed as:

$$\text{gCNR}_{\text{US}} = 1 - \left(\int_{-\infty}^{\epsilon_0} p_o(x)dx + \int_{\epsilon_0}^{\infty} p_i(x)dx \right), \quad (1)$$

where $p_i(x)$ and $p_o(x)$ are the probability density functions (PDFs) corresponding to signal powers of the target and background respectively, and ϵ_0 is the optimal decision threshold for the given image, computed from the point of intersection between $p_i(x)$ and $p_o(x)$.

Hysi *et al.* [6] demonstrated that as a consequence of photoacoustic speckle, the Nakagami-m distribution more accurately fits the envelopes of photoacoustic RF signals than the Rayleigh distribution used to model ultrasound signals. We know that the square of a Nakagami-m distributed random variable is Gamma distributed. As a result, we model the target signal power as a Gamma distribution with the PDF:

$$p_i\left(x; k, \theta\right) = \frac{x^{k-1} e^{-\frac{x}{\theta}}}{\theta^k \Gamma\left(k\right)}, \quad (2)$$

where p_i is the PDF of the target power distribution, x is the target power, and k and θ denote the shape and scale of the Gamma distribution respectively.

Thermal noise characteristic to the ultrasound receiver is a major component of noise in photoacoustic images. Thus, we retain the assumption that the the background signal power is represented with the exponential distribution [4], [7] and model the noise power as:

$$p_o\left(x; \mu\right) = \frac{1}{\mu} e^{-\frac{x}{\mu}}, \quad (3)$$

where p_o is the PDF of the background power, x is the background power, and μ is the mean noise power.

Unlike in ultrasound images, the PDFs of the target and background signal powers in photoacoustic images have up to 2 points of intersection as shown in Fig. 1. These points of intersection form the decision boundaries of the optimal classifier. Selecting the optimal decision in each region formed by these decision boundaries, we obtain the following equation for the gCNR of a photoacoustic target:

$$\begin{aligned} \text{gCNR}_{\text{PA}} \quad = \quad & 1 - \int_0^{\epsilon_0} p_i\left(x; k, \theta\right) dx \\ & - \int_{\epsilon_0}^{\epsilon_1} p_o\left(x; \mu\right) dx \\ & - \int_{\epsilon_1}^{\infty} p_i\left(x; k, \theta\right) dx. \end{aligned} \quad (4)$$

The optimal decision boundaries ϵ_0 and ϵ_1 are obtained by finding the points of intersection of the target and background signal power PDFs, resulting in the equation:

$$p_i\left(\epsilon_m; k, \theta\right) = p_o\left(\epsilon_m; \mu\right), \quad (5)$$

where $m = 0, 1$. Substituting Eq. 2 for $p_i(\epsilon_m; k, \theta)$ and Eq. 3 for $p_o(\epsilon_m; \mu)$ in Eq. 5, we obtain the equation:

$$e^{\left(\frac{1}{\theta} - \frac{1}{\mu}\right)\epsilon_m} = \left(\frac{\mu}{\theta^k + \Gamma\left(k\right)} \right) \epsilon_m^{k-1}, \quad (6)$$

which simplifies to:

$$e^{a\epsilon_m} = b\epsilon_m^c. \quad (7)$$

Equation 7 is satisfied by the LambertW function [8] as:

$$\epsilon_m = -\frac{c}{a} \times \text{LambertW}\left(\left(-\frac{a}{c}\right) \left(\frac{1}{b}\right)^{\frac{1}{c}} \right). \quad (8)$$

As Eq. 8 does not yield a simpler closed-form expression for ϵ_m, numerical values for ϵ_m are computed using the `lambertw` function in MATLAB. These values are then substituted into Eq. 4 to obtain the gCNR for the given photoacoustic image.

III. Methods

We analyzed three datasets to validate our theoretical framework with gCNR measurements across a range of channel SNR values. The first dataset contained simulated photoacoustic data from our previous publication [5]. These data were simulated with target diameters of 6 mm, 8 mm, and 10 mm using the k-Wave toolbox [9], [10]. The second dataset was acquired with a 5 mm-diameter optical fiber bundle submerged in a water bath and interfaced to a Phocus Mobile Laser (OPOTEK, Carlsbad, CA, USA). The laser was pulsed at a rate of 10 Hz with a fixed wavelength of 760 nm and laser energy at the fiber bundle tip varied from 15 mJ to 68 mJ. The setup was imaged using an Alpinion E-CUBE 12R ultrasound system (Seoul, South Korea) connected to an Alpinion L3-8 linear transducer. For the remainder of our paper, we refer to this as the experimental dataset. The third dataset consisted of *in vivo* data acquired from the hepatic vein of a *Sus domesticus* swine liver during experiments described in a previous publication from our group [11], using the photoacoustic imaging equipment described above with a laser wavelength of 750 nm and a laser energy at the fiber bundle tip of 53 mJ. Experiments were approved by the Johns Hopkins University Animal Care and Use Committee.

Normally distributed noise was added to each channel data frame in these three datasets to obtain channel SNR values in the range -40 dB to 40 dB. Photoacoustic images were created with DAS beamforming and normalized to ensure

Authorized licensed use limited to: Johns Hopkins University. Downloaded on January 14,2021 at 16:13:51 UTC from IEEE Xplore. Restrictions apply.

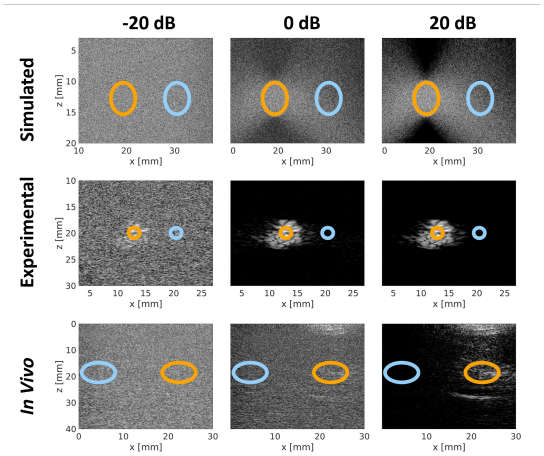

Fig. 2. Simulated, experimental, and *in vivo* photoacoustic images of targets with added noise for channel signal-to-noise ratio (SNR) values of -20 dB, 0 dB, and 20 dB, with the target and background regions of interest (ROIs) in orange and blue respectively.

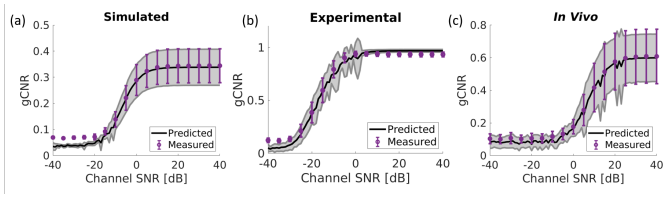

Fig. 3. The mean and standard deviation of predicted and measured generalized contrast-to-noise ratio (gCNR) as a function of channel SNR for (a) simulated targets with diameters ranging 6-10 mm, (b) a 5 mm optical fiber bundle in a water bath, and (c) an *in vivo* swine hepatic vessel.

TABLE I
MEAN ± STANDARD DEVIATION OF PREDICTED GCNR FOR SIMULATED, EXPERIMENTAL, AND IN VIVO DATASETS AT CHANNEL SNR VALUES OF -20 DB, 0 DB, AND 20 DB.

	-20 dB	**0 dB**	**20 dB**
Simulated	0.05 ± 0.01	0.28 ± 0.06	0.34 ± 0.07
Experimental	0.38 ± 0.10	0.91 ± 0.14	0.97 ± 0.01
In Vivo	0.07 ± 0.04	0.17 ± 0.05	0.56 ± 0.13

a maximum amplitude of unity. Circular regions of interest (ROIs) of equal area were used to quantify properties of the target and the background of each image. The gCNR was predicted as described in Section II. To validate the predicted gCNR values, histograms of the target and background signal powers were generated from the same ROIs with bin widths computed as described in [12]. The gCNR was then measured using Eq. 3 in [5], reproduced below for convenience:

$$\text{gCNR}_{\text{meas}} = 1 - \sum_{k=0}^{N-1} \min\{h_i(x_k), h_o(x_k)\}. \tag{9}$$

After validating our theory across variations in channel SNR, we explored the relationship among gCNR, frame averaging, and laser energy. One end of a 2 mm-diameter optical fiber bundle was inserted into a plastisol phantom, and the other end of the fiber bundle was interfaced to an LS-Series Pulsed Laser Diode (PLD) (Laser Components, Bedford, NH, USA). The PLD was pulsed at a rate of 20 Hz with a fixed wavelength of 905 nm and laser energy levels in the range 0 to 26.5 μJ. The setup was imaged using the same Alpinion scanner and L3-8 transducer as described above. The acquired channel data frames were averaged in increments 10 up to a maxium of 100 averaged frames for each laser energy. Photoacoustic images were formed with DAS beamforming from both the averaged and the individual channel data frames. The beamformed images were normalized to ensure a maximum amplitude of unity. Elliptical ROIs of equal area were used to quantify properties of the target and the background of each image. The gCNR was then predicted and measured for the photoacoustic images to quantify gCNR as functions of frame averaging and laser energy.

IV. RESULTS

Fig. 2 compares simulated, experimental, and *in vivo* results obtained with channel SNRs of -20 dB, 0 dB, and 20 dB. Each row shows improved target visibility as channel SNR increases from -20 dB to 20 dB. These improvements correspond to increases in both predicted and measured gCNR as the channel SNR increases, as reported in Table I.

Fig. 3 shows the predicted and measured gCNR as functions of channel SNR. The black lines and grey shaded regions denote the mean ± one standard deviation of the predicted gCNR for each dataset. The purple dots and error bars denote the mean ± one standard deviation of the measured gCNR for each dataset. In each dataset, we observe a sigmoidal relationship between gCNR and channel SNR. Note that no gCNR value larger than unity was measured, despite the grey shaded region crossing unity in Fig. 3 (b). Overall, the predicted gCNR strongly agreed with the measured gCNR with mean absolute errors (MAEs) of 0.032 ± 0.052, 0.057 ± 0.127, and 0.023 ± 0.033 for the simulated, experimental, and *in vivo* datasets respectively.

Fig. 4 shows the measured and predicted gCNR values as functions of the number of frames, separated by laser energy

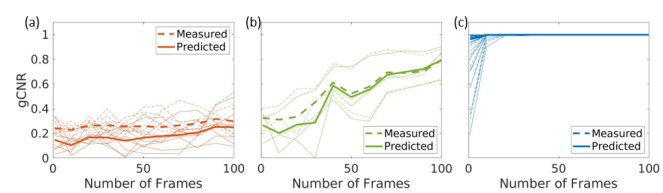

Fig. 4. Predicted and measured gCNR as functions of frame averaging computed on photoacoustic images of a 2 mm-diameter optical fiber bundle inserted into a plastisol phantom and interfaced to a Pulsed Lased Diode (PLD). The data are separated by laser energy levels in the ranges (a) 0 ± 1.91 μJ to 1.94 ± 1.39 μJ, (b) 1.56 ± 1.61 μJ to 2.35 ± 2.09 μJ, and (c) 2.00 ± 2.12 μJ to 26.47 ± 2.34 μJ. The thin solid and dashed lines denote the predicted and measured gCNR, respectively. The thick solid and dashed lines denote the mean of the thin lines for the predicted and measured gCNR, respectively.

Authorized licensed use limited to: Johns Hopkins University. Downloaded on January 14,2021 at 16:13:51 UTC from IEEE Xplore. Restrictions apply.

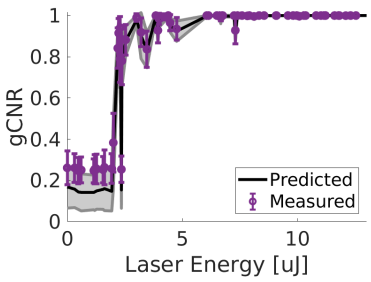

Fig. 5. Predicted and measured gCNR as functions of laser energy, obtained from images acquired with a pulsed laser diode and plastisol phantom.

levels. In Fig. 4(a), the laser energy levels (0 ± 1.91 μJ to 1.94 ± 1.39 μJ) are too low for frame averaging to significantly improve gCNR. The predicted gCNR stays between 0.105 ± 0.054 and 0.254 ± 0.092 as the number of averaged frames increases from 1 to 100. Fig. 4(b) shows mid-range laser energy levels (1.56 ± 1.61 μJ to 2.35 ± 2.09 μJ), representing cases where frame averaging is most useful with regard to improving gCNR. Fig. 4(c) shows higher laser energy levels (2.00 ± 2.12 μJ to 26.47 ± 2.34 μJ), representing cases where frame averaging is unnecessary. Here, the mean predicted gCNR begins at the high value of 0.962 ± 0.125 without frame averaging, and increases to 0.998 ± 0.012 with 10 averaged frames.

Fig. 5 shows the predicted and measured gCNR as functions of laser energy levels in the range 0 to 26.5 μJ. The predicted and measured gCNR were both small in the range 0 μJ to 1.94 μJ, with maximum values in this region of 0.168 and 0.263 respectively. Both the predicted and measured gCNR showed upward trends from 0.153 and 0.254 respectively to unity as the laser energy increased from 2.35 μJ to 7.39 μJ. Both predicted and measured gCNR saturated at unity above a laser energy level of 7.39 μJ. In addition, the gCNR predictions were observed to strongly agree with the measured gCNR for laser energy levels above 2.50 μJ. Overall, the MAE between predicted and measured gCNR values was 0.017 ± 0.041.

V. Discussion & Conclusions

The development and validation of a theoretical framework for gCNR prediction offers multiple advantages for both the designers and end-users of photoacoustic imaging systems. Reframing the design of a photoacoustic imaging system as the problem of achieving a desired gCNR with the beamformed images allows system engineers to better select parameters such as laser energy and frame averaging. With knowledge of the laser energy required to achieve a desired gCNR, design engineers can avoid unnecessarily large and bulky lasers, making their systems smaller and more suitable for surgical and interventional suites. The gCNR metric has the potential to be incorporated into the iterative design of photoacoustic imaging systems to resize system components as required. The ability to predict the behavior of gCNR with an increase in averaged frames offers engineers an additional degree of freedom to achieve desired form factors at the expense of achievable frame rates.

The gCNR predictions show promise in improving the efficiency of preoperative tasks for photoacoustic-guided surgical and interventional procedures. For example, previous work by our group studying cardiac catheterizations on *in vivo* swine required trial and error to determine the optimal laser energy for successful visual servoing during the procedure [13]. Characterizing our visual servoing system with respect to gCNR now enables us to bypass the process of trial and error and instead consider a theory-based approach to selecting desired laser energies [14].

Acknowledgments

This work is supported by the NSF CAREER Award No. ECCS-1751522 and NSF SCH Award No. NSF IIS-2014088.

References

[1] M. Patterson and F. Foster, "The improvement and quantitative assessment of b-mode images produced by an annular array/cone hybrid," *Ultrasonic Imaging*, vol. 5, no. 3, pp. 195–213, 1983.

[2] S. W. Smith, R. F. Wagner, J. M. Sandrik, and H. Lopez, "Low contrast detectability and contrast/detail analysis in medical ultrasound," *IEEE Transactions on Sonics and Ultrasonics*, vol. 30, no. 3, pp. 164–173, 1983.

[3] O. M. H. Rindal, A. Austeng, A. Fatemi, and A. Rodriguez-Molares, "The effect of dynamic range alterations in the estimation of contrast," *IEEE transactions on ultrasonics, ferroelectrics, and frequency control*, vol. 66, no. 7, pp. 1198–1208, 2019.

[4] A. Rodriguez-Molares, O. M. H. Rindal, J. D'hooge, S.-E. Måsøy, A. Austeng, M. A. L. Bell, and H. Torp, "The generalized contrast-to-noise ratio: a formal definition for lesion detectability," *IEEE Transactions on Ultrasonics, Ferroelectrics, and Frequency Control*, 2019.

[5] K. M. Kempski, M. T. Graham, M. R. Gubbi, T. Palmer, and M. A. L. Bell, "Application of the generalized contrast-to-noise ratio to assess photoacoustic image quality," *Biomedical Optics Express*, vol. 11, no. 7, pp. 3684–3698, 2020.

[6] E. Hysi, M. N. Fadhel, M. J. Moore, J. Zalev, E. M. Strohm, and M. C. Kolios, "Insights into photoacoustic speckle and applications in tumor characterization," *Photoacoustics*, vol. 14, pp. 37–48, 2019.

[7] R. Wagner, S. Smith, J. Sandrik, and H. Lopez, "Statistics of speckle in ultrasound b-scans," *IEEE Transactions on Sonics and Ultrasonics*, vol. 30, no. 3, pp. 156–163, 1983.

[8] R. M. Corless, G. H. Gonnet, D. E. Hare, D. J. Jeffrey, and D. E. Knuth, "On the lambertw function," *Advances in Computational mathematics*, vol. 5, no. 1, pp. 329–359, 1996.

[9] B. E. Treeby and B. T. Cox, "k-wave: Matlab toolbox for the simulation and reconstruction of photoacoustic wave fields," *Journal of biomedical optics*, vol. 15, no. 2, p. 021314, 2010.

[10] B. E. Treeby, J. Jaros, A. P. Rendell, and B. Cox, "Modeling nonlinear ultrasound propagation in heterogeneous media with power law absorption using ak-space pseudospectral method," *The Journal of the Acoustical Society of America*, vol. 131, no. 6, pp. 4324–4336, 2012.

[11] K. M. Kempski, A. Wiacek, M. Graham, E. González, B. Goodson, D. Allman, J. E. Palmer, H. Hou, S. Beck, J. He, and M. A. L. Bell, "In vivo photoacoustic imaging of major blood vessels in the pancreas and liver during surgery," *Journal of biomedical optics*, vol. 24, no. 12, p. 121905, 2019.

[12] M. Wand, "Data-based choice of histogram bin width," *The American Statistician*, vol. 51, no. 1, pp. 59–64, 1997.

[13] M. Graham, F. Assis, D. Allman, A. Wiacek, E. Gonzalez, M. Gubbi, J. Dong, H. Hou, S. Beck, J. Chrispin, and M. A. L. Bell, "In vivo demonstration of photoacoustic image guidance and robotic visual servoing for cardiac catheter-based interventions," *IEEE transactions on medical imaging*, vol. 39, no. 4, pp. 1015–1029, 2019.

[14] M. A. L. Bell, "Photoacoustic imaging for surgical guidance: Principles, applications, and outlook," *Journal of applied physics*, vol. 128, no. 6, p. 060904, 2020.

Authorized licensed use limited to: Johns Hopkins University. Downloaded on January 14,2021 at 16:13:51 UTC from IEEE Xplore. Restrictions apply.